NeuroImage 189 (2019) 202–213

Contents lists available at ScienceDirect

NeuroImage

journal homepage: www.elsevier.com/locate/neuroimage

Quantifying amide proton exchange rate and concentration in chemical exchange saturation transfer imaging of the human brain

Hye-Young Heo [a,b,*], Zheng Han [a,b], Shanshan Jiang [a], Michael Schär [a], Peter C.M. van Zijl [a,b], Jinyuan Zhou [a,b]

[a] Division of MR Research, Department of Radiology, Johns Hopkins University, Baltimore, MD, USA
[b] F.M. Kirby Research Center for Functional Brain Imaging, Kennedy Krieger Institute, Baltimore, MD, USA

ARTICLE INFO

Keywords:
CEST
APT
Exchange rate
Concentration
MR fingerprinting

ABSTRACT

Current chemical exchange saturation transfer (CEST) neuroimaging protocols typically acquire CEST-weighted images, and, as such, do not essentially provide quantitative proton-specific exchange rates (or brain pH) and concentrations. We developed a dictionary-free MR fingerprinting (MRF) technique to allow CEST parameter quantification with a reduced data set. This was accomplished by subgrouping proton exchange models (SPEM), taking amide proton transfer (APT) as an example, into two-pool (water and semisolid macromolecules) and three-pool (water, semisolid macromolecules, and amide protons) models. A variable radiofrequency saturation scheme was used to generate unique signal evolutions for different tissues, reflecting their CEST parameters. The proposed MRF-SPEM method was validated using Bloch-McConnell equation-based digital phantoms with known ground-truth, which showed that MRF-SPEM can achieve a high degree of accuracy and precision for absolute CEST parameter quantification and CEST phantoms. For *in-vivo* studies at 3 T, using the same model as in the simulations, synthetic Z-spectra were generated using rates and concentrations estimated from the MRF-SPEM reconstruction and compared with experimentally measured Z-spectra as the standard for optimization. The MRF-SPEM technique can provide rapid and quantitative human brain CEST mapping.

1. Introduction

Chemical exchange saturation transfer (CEST) imaging is an important molecular MRI technique that can generate contrast based on the proton exchange between labeled protons in solutes and free bulk water protons, or on the water exchange between solute-bound water and free bulk water in tissue (Goffeney et al., 2001; Ward et al., 2000). CEST-MRI was developed to indirectly detect various endogenous low-concentration mobile biomolecules with water-exchangeable protons, such as proteins and peptides (van Zijl et al., 2003; Zhou et al., 2003b); glutamate (Cai et al., 2012); creatine (Haris et al., 2014); glycogen (van Zijl et al., 2007); and glycosaminoglycans (Ling et al., 2008); exogenous-specific molecular imaging agents (Aime et al., 2005; Walker-Samuel et al., 2013; Zhang et al., 2001); as well as tissue physiological parameters, including temperature (Zhang et al., 2005) and pH (Sun et al., 2007; Zhou et al., 2003b). Currently, CEST-MRI holds great promise for abundant clinical molecular imaging applications (Jiang et al., 2017; Jones et al., 2017; Li et al., 2014; Zhang et al., 2016a, 2017a; Zhou et al., 2013b).

Most current CEST-MRI protocols acquire CEST-weighted images that reflect a few other contributions, including residual magnetization transfer contrast (MTC) and residual tissue relaxation characteristics (Xu et al., 2014b; Zaiss et al., 2011; Zhou et al., 2008), thus limiting the assessment of quantitative proton exchange rates and concentrations. In addition, inconsistent and controversial results have been reported by different research groups due to the choice of different CEST metrics (Heo et al., 2017a; Xu et al., 2014b; Zaiss et al., 2011), reference images (Cai et al., 2015; Heo et al., 2016c; Jin et al., 2013; Jones et al., 2013; Zhou et al., 2003b), and different experimental parameters (Heo et al., 2017c; Sun et al., 2013; Zhao et al., 2011; Zhou et al., 2013a). Investigators in the CEST community have a great interest in quantifying label proton concentrations and exchange rates. One of the most promising CEST quantification methods is to fit CEST signals obtained from repeated and serial image acquisition with varied saturation powers, as well as saturation frequency offsets to the steady-state analytical solution of the Bloch-McConnell equation (Geades et al., 2017; Heo et al., 2016c;

* Corresponding author. Division of MR Research, Department of Radiology, Johns Hopkins University School of Medicine, 600 N. Wolfe Street, Park 334, Baltimore, MD, 21287, USA.
E-mail address: hheo1@jhmi.edu (H.-Y. Heo).

https://doi.org/10.1016/j.neuroimage.2019.01.034
Received 27 December 2017; Received in revised form 9 January 2019; Accepted 13 January 2019
Available online 14 January 2019

Liu et al., 2013; McMahon et al., 2006; Woessner et al., 2005; Zhou et al., 2004). The acquisition of multi-sampled Z-spectra, i.e., acquisitions at multiple B_1 or saturation time settings, allows analysis by model-based fitting of the CEST process. The simplest CEST model-based analysis consists of two pools, free bulk water protons and single solute protons. However, MTC effects from semisolid macromolecular protons *in-vivo* interfere with the CEST process (Desmond and Stanisz, 2012; Heo et al., 2016b; Hua et al., 2007; van Zijl and Yadav, 2011). Incorporating multiple pools in the model-based analysis is challenging because it requires more parameters that must be fitted from the data, leading to a higher risk of over-fitting errors, and thus, inaccurate quantification results. In addition, the use of multiple RF saturation frequencies under varied RF saturation powers requires long scan times, which is a major obstacle to clinical translation.

MR fingerprinting (MRF) is a new approach for efficient multiple tissue parameter mapping with varying pulse sequence parameters of interest in a pseudorandom manner (Cohen et al., 2018; Liao et al., 2017; Ma et al., 2013, 2017; Su et al., 2017; Wang et al., 2017; Zhou et al., 2018). Typically, a pattern-matching algorithm is used to find different tissue-type parameters against a pre-calculated database, a so-called "dictionary," from Bloch equation simulations with a wide variety of tissue parameter combinations. Therefore, MRF has been shown to be robust to severe aliasing artifacts from highly undersampled k-space measurements due to the incoherent sampling and the nature of a matching procedure based on prior information. When multiple components for CEST-MRI are considered, however, it requires even more parameters that must be matched from the dictionary, possibly leading to erroneous quantification results. Furthermore, the size of the database would have to be dramatically increased and an exhaustive search performed, limiting practical application.

In this study, we developed a dictionary-free MRF technique to allow CEST quantification with a reduced data set by using the simplifying assumption of subgrouping proton exchange models (MRF-SPEM). As a first example of application to amide proton transfer (APT) MRI (Zhou et al., 2003a, 2003b), we assumed two-pool (water and semisolid macromolecules) and three-pool (water, semisolid macromolecules, and amide protons) models. A variable RF saturation scheme was used to generate uncorrelated signal evolutions for different tissue properties. Carefully designed frequency sampling and RF saturation power variation further allowed quantification in terms of group-based average exchange rates and apparent concentrations at a certain amide proton frequency. The MRF-SPEM method was validated using Bloch-McConnell equation-based digital phantoms with known ground-truth values. For *in-vivo* studies, synthetic Z-spectra were generated by inserting CEST quantities obtained from MRF-SPEM reconstruction into the forward Bloch transform. These were compared with measured Z-spectra as the standard due to the lack of an objective ground-truth or gold standard *in-vivo*.

2. Methods

2.1. MRF-SPEM acquisition

In the MRF-SPEM framework, RF saturation frequency offsets (Ω), saturation power (B_1), saturation duration (Ts), and repetition time (TR) were varied throughout the acquisition, generating unique signal evolutions for different tissue properties, as shown in Fig. 1. TRs were varied according to Ts, but relaxation delay (Td) and turbo spin echo (TSE) acquisition (Ta) times were fixed (TR = Ts + Ta + Td). For APT quantification, MRF-SPEM images consisted of two distinct datasets: (1) MTC data with far off-resonance frequency offsets between 10 ppm and 50 ppm (black crosses in Fig. 2a); and (2) APT-weighted data with saturation frequency offsets between 3 ppm and 4 ppm (red crosses in Fig. 2a). The far off-resonance frequency offsets were chosen to sample MTC data points and to avoid possible downfield CEST and upfield nuclear Overhauser enhancement (NOE) signal contributions to water

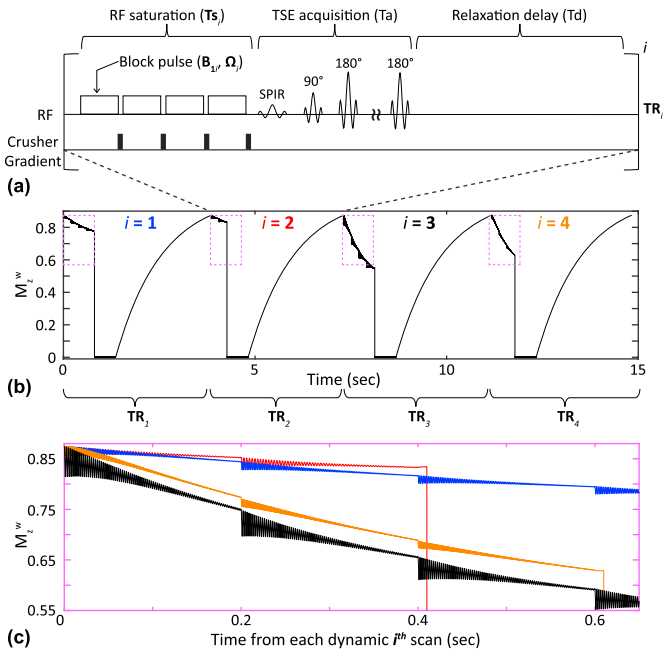

Fig. 1. (a) An illustration of turbo spin-echo (TSE)-based CEST sequence with four (i = 4) dynamic scans. A saturation pulse train consists of block pulses of 200 ms duration each with a 10 ms delay between them. (SPIR = spectral presaturation with inversion recovery). (b) The evolution of the longitudinal magnetization of the water (M_z^w) with varied saturation parameters, where Ω_i = 4, 3, 3.5, 10 ppm, B_{1i} = 1.2, 0.8, 2, 3 μT, Ts_i = 800, 400, 800, 600 ms, and TR_i = 3.5, 3.08, 3.5, 3.29 s, respectively. (c) Zoomed-in displays (pink boxes in b) showing distinct saturation effects. All initial magnetizations for each dynamic scan are identical due to the fixed relaxation delay time.

saturation originating from mobile proteins and peptides. These data were fitted to a two-pool MTC exchange model, while APT-weighted data acquired at RF saturation frequency offsets around 3.5 ppm were fitted to the three-pool exchange model. The two-pool parameters were incorporated into the three-pool model as prior known information, reducing the number of parameters and fitting uncertainty errors. In addition, fast-exchanging amine protons around 3 ppm in glutamate (Cai et al., 2012), hydroxyl protons around 1 ppm in myo-inositol (Haris et al., 2011), glycogen (van Zijl et al., 2007), glycosaminoglycans (Ling et al., 2008), side-chain amide or guanidinium protons around 2 ppm in proteins (Zhang et al., 2017d; Zhou et al., 2003a), and guanidinium protons in creatine (Cai et al., 2015; Haris et al., 2012) may make contributions to the APT-weighted signals. At lower RF saturation power, CEST effects are dominated by slowly exchanging amide protons, whereas, at higher B_1, this is taken over by fast-exchanging amine and hydroxyl protons (Heo et al., 2017b; Jin et al., 2012; van Zijl et al., 2018). Based on this theory, relatively low B_1 powers between 0.5 μT and 1.2 μT were applied in an attempt to isolate APT signals from the broad resonances of rapidly exchangeable protons.

2.2. Bloch-McConnell simulations

Three-pool, Bloch-McConnell equation-based simulations were performed to simulate MRF-SPEM signal profiles. All longitudinal magnetization evolutions were analytically simulated following a single-shot TSE sequence, as shown in Fig. 1. MRF-SPEM profiles were generated with a schedule of Ω, B_1, Ts, and TR, and were used for digital phantoms that consisted of two compartments (C1 and C2) with different exchange rates and concentration parameters for CEST and MTC contributions. Before simulating MRF-SPEM Z-spectra, four dummy scans were employed to achieve steady-state. The parameters (C1/C2) used for the simulation are shown in Table 1 (left two columns). Furthermore, T_2

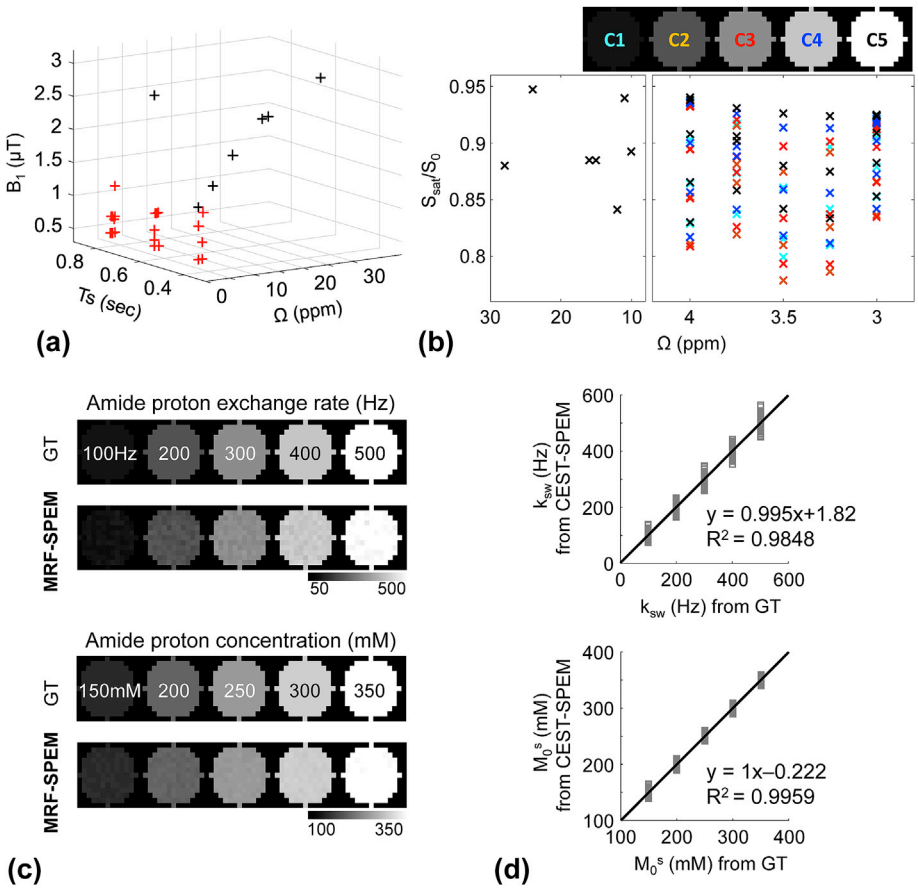

Fig. 2. (a) An example of Ω, B_1, and Ts schedules for an MRF-SPEM acquisition. Black crosses are for two-pool MTC model-fitting (10 ppm < Ω < 50 ppm and 1.2 μT < B_1 < 3 μT) and red crosses (3 ppm < Ω < 4 ppm and 0.5 μT < B_1 < 1.2 μT) are for three-pool model-fitting. (b) MRF-SPEM signal profiles obtained from five compartments with varied proton exchange rates and concentrations listed in (c). (c) Pixel-wise maps of the proton exchange rate (k_{sw}, Hz) and concentration (M_0^s, mM) in digital phantoms (SNR = 100) with the variable RF saturation schedules as shown in (a). (c) Correlation plots comparing proton exchange rates (top) and concentrations (bottom) between MRF-SPEM reconstruction values and ground-truth (GT) phantom values.

Table 1
Ground truth values of the three-pool exchange model and estimated parameters (mean ± standard deviation) from MRF-SPEM in the numerical phantom study.

	Ground Truth		MRF-SPEM	
	C1	C2	C1	C2
T_{1w} (sec)	1.20	1.40	1.20 ± 0.00	1.40 ± 0.00
k_{mw} (Hz)	20	20	20 ± 0	20 ± 1
M_0^m (M)	11.0	4.4	10.9 ± 0.0	4.4 ± 0.2
k_{sw} (Hz)	300	70	301 ± 2	72 ± 2
M_0^s (mM)	150	250	149 ± 0	246 ± 0

Other simulation parameters are shown in the Method section.

values were assumed equal in both compartments, namely 65 ms for water and amide protons and 20 μs for MTC protons. The chemical shifts of water, MTC, and amide protons were 0 ppm, 0 ppm, and 3.5 ppm, respectively. B_0 and B_1 fields were assumed to be homogenous. For comparison with magnetization transfer ratio asymmetry (MTR_{asym}) analysis, conventional Z-spectra were also generated at the RF frequency offset ranging from −6 to +6 ppm for saturation powers of 0.5, 1, 1.5, 2, and 3 μT, and a saturation duration of 800 ms (a series of four block RF saturation pulses, 200 ms duration each). A Bland-Altman analysis was performed to evaluate the agreement between MRF-SPEM and ground-truth phantom values. For all simulations, Rician noise was added to generate noisy images or profiles. We estimated an apparent standard deviation of ~855, scaled by a factor of 1/0.655 to account for the Rician noise distribution from a background region, and an average signal of 97138 from a white matter region in saturated MRF-SPEM images at 3.5 ppm (SNR of ~113). For the digital phantom study, we used a SNR level of 100 with the pseudo-random Rician noise samples which were generated by using conventional inverse transform sampling. The concentration of the water protons (110 M) was used to convert the semisolid macromolecular and amide protons concentrations from relative to absolute units for simulation, phantom, and in-vivo human studies.

2.3. Phantom experiments

Ammonium chloride (NH_4Cl, Sigma Aldrich, St Louis, MO, USA) phantoms were prepared in 50 mL tubes by dissolving 1.07 g (500 mM) or 2.14 g (1M) ammonium chloride in 40 mL PBS (pH 7.0), followed by titration to pH of 4.5, 4.6, and 5.0 using NaOH solution and a pH meter. To mimic the MTC pool, 1% agarose (low gelling temperature, Sigma Aldrich, St Louis, MO, USA) was added to tubes, which was heated briefly using microwave to dissolve agarose. Tubes were then bound using tapes and placed in a plastic container. The container was then filled with heated water containing 1% agarose, which was allowed to gel before scan. All studies were performed on a 3 T Philips Achieva MRI system (Best, Netherlands) with a 32-channel element head coil, and all reconstruction algorithms were implemented in MATLAB R2017 (The MathWorks, Inc., Natick, MA). For CEST imaging, three sets of imaging parameters were adopted. First, conventional Z-spectrums were acquired with 161 frequency offsets between −20 and 20 ppm at intervals of 0.25 ppm with RF saturation powers of 1, 1.5, 2, 2.5, and 3 μT. The scan time was 47.6 min. Second, densely sampled Z-spectrums were acquired with 94 frequency offsets between 1.5 and 3.5 ppm at intervals of ~0.0234 ppm and between 8 and 20 ppm at intervals of 1 ppm with RF saturation powers of 1, 1.5, 2, 2.5, 3, and 3.5 μT. The scan time was 33.6 min. Third, MRF-SPEM profiles were acquired at 26 frequency offsets between 1.5 and 3.5 ppm for three-pool CEST fitting and 5 frequency offsets between 10 and 20 ppm for two-pool MTC fitting with RF saturation powers ranging from 1 to 3 μT and RF saturation times ranging from 400 to 800 ms. The scan time was 1.9 min. Unsaturated images were also acquired for signal normalization. Additionally, water saturation

shift-referencing (WASSR) (Kim et al., 2009) (26 frequency offsets from −1.2–1.2 ppm at intervals of 0.125 ppm, B_1 of 0.5 μT) and dual-TR (TR = 20 and 120 ms) data were acquired for B_0 and B_1 corrections, respectively.

2.4. In-Vivo MRI experiments

Human studies were approved by the Johns Hopkins Institutional Review Board. Five healthy volunteers (women, n = 2; men, n = 3; age, 32.6 ± 4.0) were recruited, who provided written, informed consent for the study. MRF-SPEM image data were obtained from a fat-suppressed (spectral pre-saturation with inversion recovery, SPIR), single-shot TSE pulse sequence using the following parameters: TE = 6.4 ms; FOV = 212 × 186 mm^2; acquisition and reconstruction resolution = 2.2 × 2.2 × 4.4 and 0.83 × 0.83 × 4.4 mm^3; turbo spin-echo factor = 45; and single slice acquisition. WASSR and dual-TR data were also acquired with the same parameters used for the ammonium chloride phantom and incorporated into the MRF-SPEM reconstruction framework for B_0 and B_1 corrections, respectively. The MRF-SPEM was also compared to the extrapolated semisolid magnetization transfer reference (EMR) method (Heo et al., 2016a, 2016c; Lee et al., 2017). For EMR data acquisitions, the frequency sweep corresponded to full Z-spectra with the following frequency offsets: unsaturated (S_0), 0 to ± 6 ppm at intervals of 0.5 ppm; + 7 ppm to + 20 ppm at intervals of 1 ppm; + 25 ppm to + 50 ppm at intervals of 5 ppm; and 60 ppm. Three RF saturation powers (1, 1.5, and 2 μT) were applied. Total EMR scan time was 11.2 min.

2.5. MRF-SPEM processing

For motion correction, all MRF-SPEM datasets were registered to the first saturated image using a rigid body transformation algorithm with a mutual information cost function and bicubic resampling (Zhang et al., 2016b). Then, we fitted MRF-SPEM data with the above-described two- and three-pool, Bloch-McConnell equation-based proton exchange models using a nonlinear least-squares fitting approach, which was implemented using the Levenberg-Marquardt algorithm. The three-pool exchange model, including the free bulk water proton pool (w), the water exchangeable solute proton pool (s), the semisolid macromolecular proton pool (m), and the magnetization in each pool (M^w, M^s, and M^m) in the presence of exchange and RF irradiation, can be described in matrix format by (Heo et al., 2016c; Woessner et al., 2005; Zhou and van Zijl, 2006; Zhou et al., 2004):

$$\frac{dM(t)}{dt} = A(t)M(t) + B \quad [1]$$

where

$$A(\omega_1) = \begin{bmatrix} D_w & N_{ws} & N_{wm} \\ N_{sw} & D_s & N_{sm} \\ N_{mw} & N_{ms} & D_m \end{bmatrix} \quad [2]$$

$$D_i = \begin{bmatrix} -k_{2i} & -(\omega - \omega_i) & 0 \\ (\omega - \omega_i) & -k_{2i} & -\omega_1 \\ 0 & \omega_1 & -k_{1i} \end{bmatrix} \quad [3]$$

$$N_{ij} = k_{ij}\begin{bmatrix} 1 & 0 & 0 \\ 0 & 1 & 0 \\ 0 & 0 & 1 \end{bmatrix} \quad [4]$$

$$B = [B_w \;\; B_s \;\; B_m]^T \quad [5]$$

$$B_i = \begin{bmatrix} 0 & 0 & M_0^i R_{1i} \end{bmatrix}^T \quad [6]$$

where ω_1 is the RF saturation amplitude; ω is the RF saturation frequency; ω_i is the resonance frequency of pool i; k_{ij} represents the proton exchange rate from pool i to pool j; R_{1i} and R_{2i} are the longitudinal and transverse relaxation rate of pool i, respectively; $k_{1/2w}$, $k_{1/2s}$, and $k_{1/2m}$ are given by $R_{1/2w} + k_{ws} + k_{wm}$, $R_{1/2s} + k_{sw}$, and $R_{1/2m} + k_{mw}$, respectively; and M_0^i is the equilibrium magnetization of pool i. The analytical solution of the coupled linear differential equations (Eq. [1]) is:

$$M = \left(M_0 + BA^{-1}\right)e^{At} - BA^{-1} \quad [7]$$

where

$$M_0 = \begin{bmatrix} M_0^w & M_0^s & M_0^m \end{bmatrix}^T \quad [8]$$

$$M_0^i = \begin{bmatrix} 0 & 0 & M_0^i \end{bmatrix}^T \quad [9]$$

The longitudinal magnetization evolution was generated based on a pulse-train CEST sequence with a single-shot TSE readout. Crusher gradients of 10-ms duration were applied between block RF saturation pulses to suppress residual transverse magnetization by setting zero transverse magnetization components (spoiler matrix). For the image acquisition, the magnetization vector evolution was calculated by multiplying the previous magnetization vectors with the rotation matrices to consider a 90° excitation pulse followed by a 180° refocusing pulse and multiple refocusing pulses forming echo trains. During the relaxation delay period, the magnetization vector was calculated solely by relaxation recovery process in the absence of B_1. The three-pool APT exchange model can be reduced to the two-pool MTC exchange model (free bulk water + semisolid macromolecular proton pools) by assuming the concentration of amide proton pools to be zero. The RF saturation parameters and repetition times corresponding to saturation schedules were updated for each dynamic scan. The three-pool APT exchange model was analytically solved with the *a priori* fitted two-pool symmetric MTC parameters obtained from far off-resonance frequency offsets and the parameter fitting was performed using the minimum norm estimate. Our model fitting approach substantially reduced the risk of over-fitting and the uncertainties of direct three-pool model parameter estimates. The quality of the estimated parameters was evaluated by the root of the sum of the squared difference between the fitted and acquired MRF-SPEM data, and the χ^2 goodness-of-fit metric. In the fitting process, the values of the parameters were constrained within upper and lower bounds of [0.1, 3.5 s] for T_{1w}, [0.01, 2 s] for T_{2w}, [1, 200 μsec] for T_{2m}, [1, 200 Hz] for k_{mw}, [1, 20 M] for M_0^m, [0.1, 500 msec] for T_{2s}, [1, 600 Hz] for k_{sw}, [1, 600 mM] for M_0^s for in-vivo studies, but adjusted for simulation and phantom studies. B_0 shifts and B_1 scaling factors obtained from the additional WASSR and B_1 calibration scans were applied pixel-wise during the fitting.

In addition, Monte-Carlo simulation studies were performed to compare MRF-SPEM and MRF (one-step fitting) methods with simulated MRF-SPEM signal profiles. 1000 sets of noisy images (SNR of ~100) were generated with different parameters of the semisolid macromolecular proton and amide proton pools. For each trial, the pool parameters were randomly chosen within the range of k_{mw} from 20 to 60 Hz at intervals of 0.25 Hz, the range of M_0^m from 4 to 12 M at intervals of 0.05 M, the range of k_{sw} from 50 to 500 Hz at intervals of 2.5 Hz, and the range of M_0^s from 100 to 400 mM at intervals of 2 mM.

2.6. Validation of MRF-SPEM using synthetic CEST data

A "true" gold standard does not currently exist for absolute CEST quantification of *in-vivo* brain tissue. Instead, synthetic Z-spectra (or CEST signals) were generated using CEST parameters obtained from the MRF-SPEM methodology and then, were compared with experimental measurements. Virtual scanner settings (e.g., TR, TE, TSE factor, excitation flip angles, Ω, B_1, Ts, etc.) that corresponded to the experimental measurements were used. For a direct comparison with the standard, synthesized $APT^{\#}$ signal intensities were calculated by:

$$APT^{\#}(syn) = Z_{ref}(+3.5ppm) - Z_{lab}(+3.5ppm) \quad [10]$$

where Z_{ref} and Z_{lab} are the reference image signal intensity and label image signal intensity normalized with respect to the image signal intensity measured without RF saturation, respectively. For APT$^{\#}$(syn) calculation, Z_{ref} and Z_{lab} were calculated by using the Bloch-McConnell equation with two-pool and three-pool exchange models, respectively, with parameters obtained from MRF-SPEM. By assuming the concentration of a solute proton pool to be zero ($M_0^s = 0$), the three-pool model (Z_{lab}) can be reduced to the two-pool model (Z_{ref}).

For the validation standard, reference and labeled Z-spectra were taken from the extrapolated semisolid MT reference (EMR) signal (namely, Z_{EMR}) and the B_0-corrected experimental Z-spectra (Z_{exp}), respectively:

$$APT^{\#}(meas) = Z_{EMR}(+3.5ppm) - Z_{exp}(+3.5ppm) \quad [11]$$

The EMR calculation was performed according to the procedures based on recently published papers (Heo et al., 2016c, 2018). Wide-offset experimental Z-spectra with MTC data points between 8 and 60 ppm were chosen to avoid the interference of possible CEST and upfield NOE signals from mobile proteins and peptides and were fitted to a two-pool MTC model with a symmetric Lorentzian lineshape. The experimental MTC datasets acquired at three RF saturation powers (1, 1.5, and 2 μT) were simultaneously fitted to improve the EMR fitting quality. Then, the MTC and direct water saturation contributions were extrapolated to obtain baseline signals (Z_{EMR}) at the respective RF saturation frequencies of interest (e.g., 3.5 ppm). To compare APT$^{\#}$(syn) results with the experimental measurement, APT$^{\#}$(meas), two ROIs enclosing the gray matter (GM) and white matter (WM) were analyzed. These ROIs were carefully drawn on the unsaturated S_0 image. Data in graphs and tables are presented as mean ± standard deviation. Statistical analysis was performed using a one-way analysis of variance, followed by Tukey's post hoc test. Statistical significance was considered at $p < 0.05$.

3. Results

3.1. Bloch-McConnell simulation results

The longitudinal magnetization of free bulk water (M_z^w) was changed dynamically under a variable RF saturation scheme (Ω, B_1, Ts, and TR), generating unique magnetization signals. Fig. 2a shows the pattern of RF saturation parameters varied deliberately throughout the saturation, producing dynamic CEST-weighted images (red crosses) and MTC-weighted images (black crosses) where the magnitude of the MR signal of each voxel changed at every dynamic step (Fig. 2b). Based on our digital phantom studies (Fig. 2c) at an appropriate SNR level of 100 (SNR for WM measured is 113), excellent agreement was observed for MRF-SPEM and the known exchange rate and concentration (ground-truth values). As shown in Fig. 2d, the results show a strong linear correlation ($R^2 = 0.985$ for k_{sw}; $R^2 = 0.996$ for M_0^s), with slopes of 0.995 for k_{sw} and 1.000 for M_0^s. The y-intercepts were 1.82 Hz for k_{sw} and −0.222 mM for M_0^s. For k_{sw}, the 95% limits of agreement were −34 Hz to 35 Hz, with a mean bias of 0.38 Hz. For M_0^s, the 95% limits of agreement were −9 mM to 8.7 mM, with a mean bias of −0.17 mM (also see Fig. 3). A Bland-Altman analysis was performed to assess the agreement between MRF-SPEM reconstruction and ground-truth values at different SNR levels (Fig. 3). The analysis revealed no significant bias for the measurement of k_{sw} and M_0^s over all SNR levels. However, the 95% limits of agreement became narrow and fewer outliers were present at higher SNRs. Monte-Carlo simulations were used to assess the precision and accuracy of two-pool MTC and solute proton parameter estimation by MRF-SPEM and MRF methods as shown in Fig. 4. The parameters estimated from MRF-SPEM were more accurate (close to ground truth) and precise (narrow distribution) than MRF method.

Fig. 5 shows another Bloch simulation result for the digital phantom with two compartments (C1 and C2 mimicked normal tissue and lesion, respectively). The parameters of the compartments are shown in Table 1. Interestingly, there was a negligible MTR_{asym} (3.5 ppm) signal difference between the two compartments at an RF saturation power of 1 μT (Fig. 5b and d), despite the different water relaxation rates, MTC (except for semisolid macromolecular proton exchange rate), and CEST parameters. Furthermore, the strong RF saturation power dependency of MTR_{asym} (3.5 ppm) image contrast can be seen clearly in Fig. 5b and d. A positive MTR_{asym} (3.5 ppm) image contrast between compartments C2 and C1 was observed at low RF power (0.5 μT) due to small MTC and direct saturation effects and the smaller exchange rate in C2 having close to maximal saturation. The MTR_{asym} (3.5 ppm) image contrast between two compartments became negative at higher RF saturation powers (>1 μT) because the solute exchange rate of C1 was faster than that of C2 and the small APT effect in C2 was overwhelmed by the MTC and direct

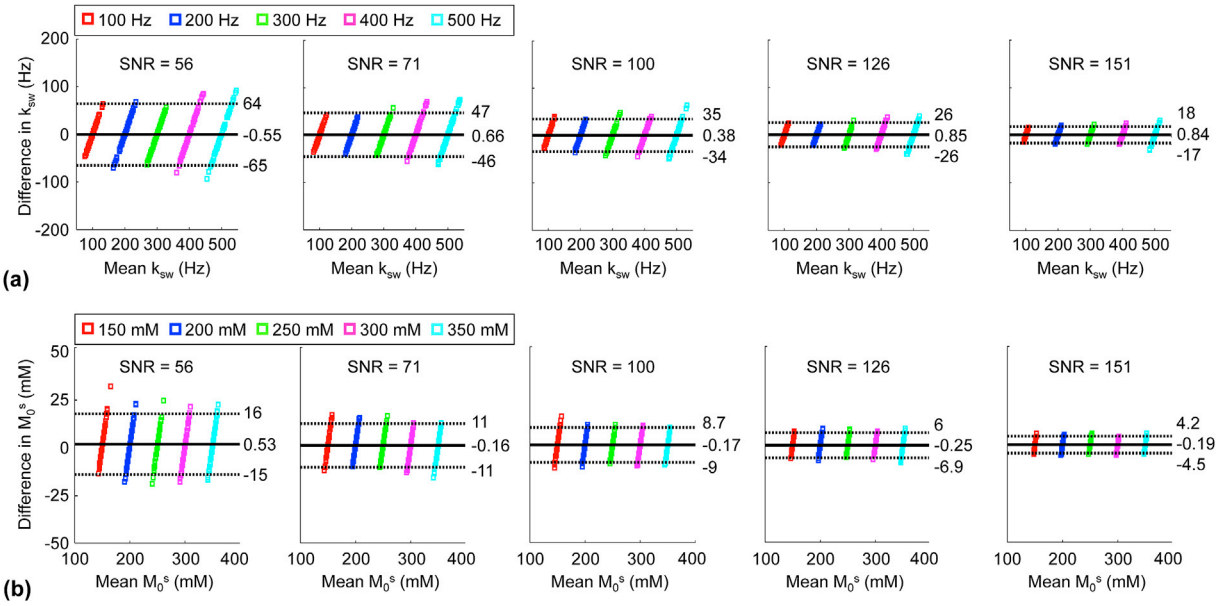

Fig. 3. Bland-Altman plots comparing proton (a) exchange rates and (b) concentrations between MRF-SPEM reconstruction values and ground-truth phantom values at different SNR levels. The 95% limits of agreement are indicated by dotted black lines, and the mean bias is indicated by the solid black line.

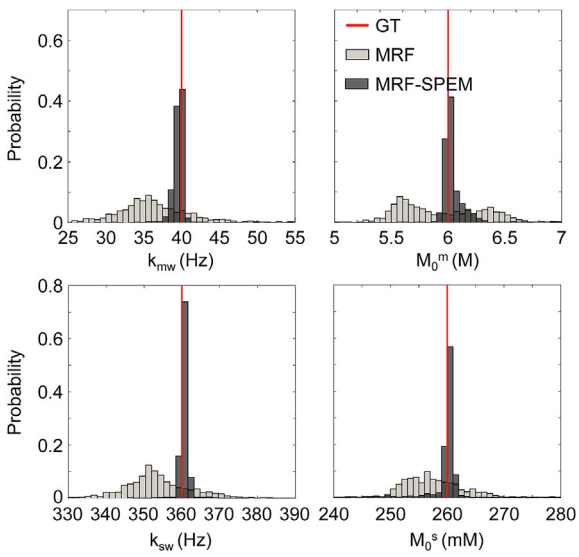

Fig. 4. Monte-Carlo simulation results (1000 trials) comparing the MRF-SPEM and MRF methods.

saturation effects. When using the variable RF saturation scheme, image voxels with different relaxation rates, water-exchangeable proton concentrations, and exchange rates evolved differently, thereby generating unique magnetization trajectories, as shown in Fig. 5c. Accurate and precise parameters (Fig. 5e) were successfully decoded, which were in excellent agreement with the ground-truth values (Table 1).

3.2. CEST phantom imaging results

Fig. 6 shows ammonium chloride phantom results. The phantom consists of four compartments with either varying NH_4Cl concentration or pH (Fig. 6a). RF saturation power dependencies of the direct water saturation, semisolid MTC, and CEST signals can be seen clearly as shown in Fig. 6b and c. Instead of using a repeated and serial image acquisition with varied saturation powers and saturation frequency offset, a variable RF saturation and acquisition created unique signal evolutions (Fig. 6d) for the compartments with different CEST concentrations or pH. Fig. 6e shows the image contrast of MTR_{asym} (2.5 ppm) between vials. However, it is not clear what the contribution (proton exchange rate or concentration) is of the underlying contrast on the observed CEST-weighted images. Quantitative CEST parameter maps obtained from the conventional Bloch equation fitting method which is a two-step fitting approach

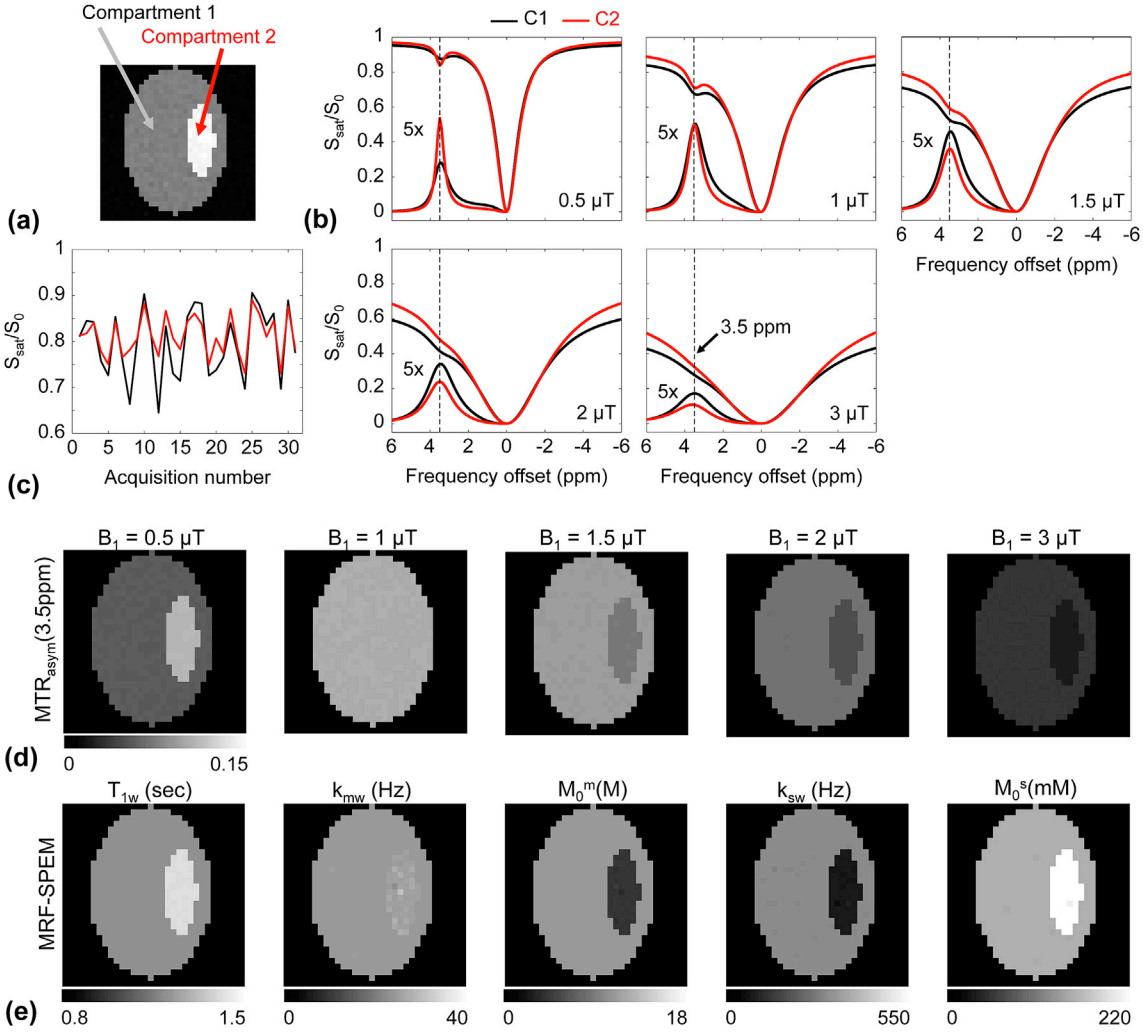

Fig. 5. (a) Two homogenous compartments (C1 and C2) in a digital phantom (SNR = 100) having different water T_1 relaxation times, semisolid macromolecular proton concentrations, solute proton exchange rates, and concentration values, as shown in Table 1. (b) Conventional Z-spectra and MTR asymmetry curves at different RF saturation powers. (c) Unique MRF-SPEM signal evolution profiles obtained from two compartments. (d) MTR_{asym} (3.5 ppm) image contrasts under different RF saturation powers. (e) water, MTC, and solute proton quantitative maps. Note that the semisolid macromolecular proton exchange rates in both compartments are identical.

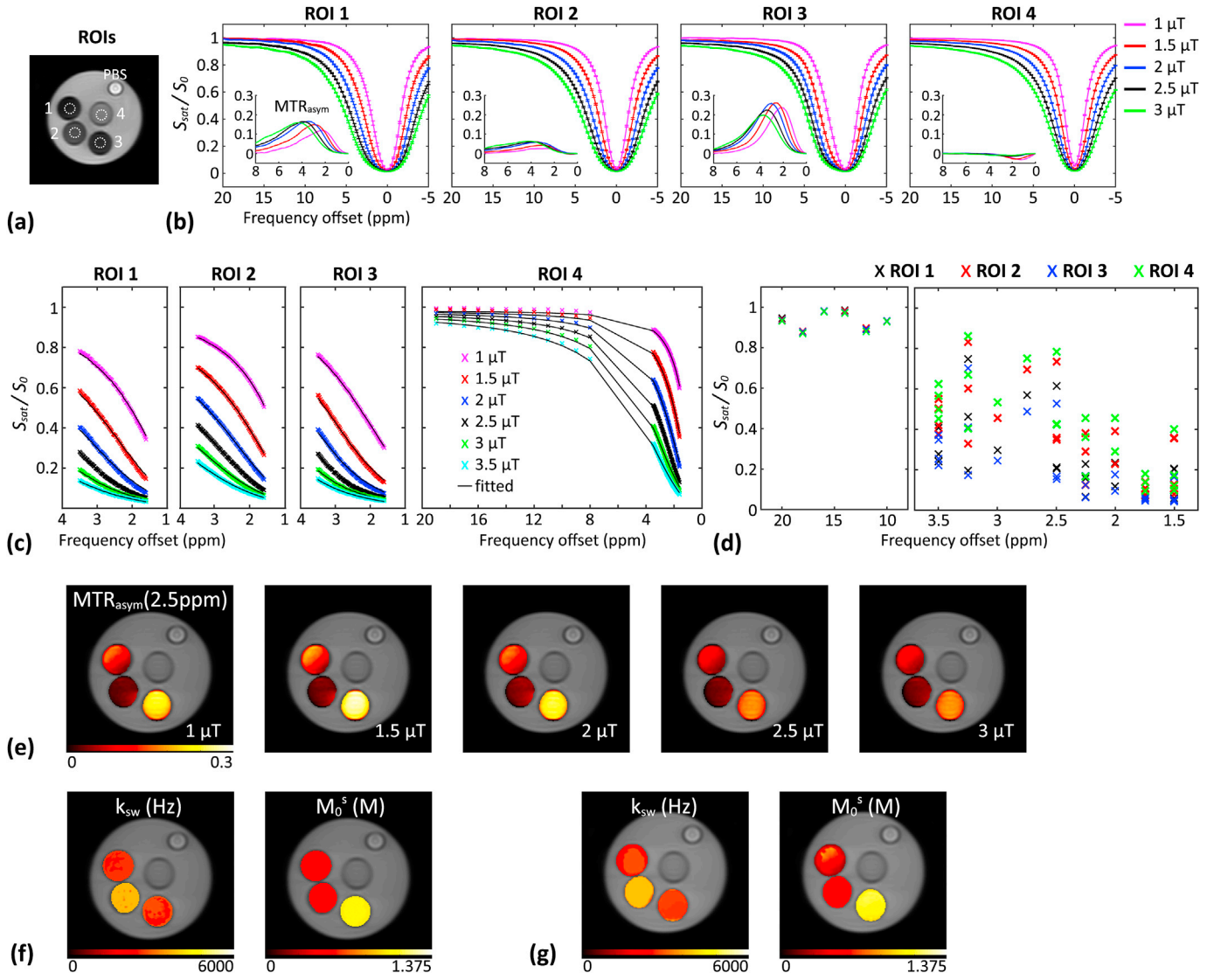

Fig. 6. CEST phantom validation experiments. (a) a phantom with four compartments: (i) pH 4.5, 0.5 M NH_4Cl + 1% agarose + PBS, (ii) pH 5.0, 0.5 M NH_4Cl + 1% agarose + PBS, (iii) pH 4.6, 1 M NH_4Cl + 1% agarose + PBS, and (iv) pH 7.0, 1% agarose + PBS. (b) Z-spectra and MTR_{asym} curves, (c) densely sampled Z-spectra, and (d) MRF-SPEM signals obtained from four ROIs. (e) MTR_{asym} (2.5 ppm) maps with RF saturation powers of 1, 1.5, 2, 2.5, and 3 μT. Quantitative CEST parameter maps from (f) the conventional three-pool Bloch-equation fitting method using the densely sampled Z-spectra as shown in (c) and (g) MRF-SPEM reconstruction using the MRF-SPEM signal profiles as shown in (d).

(two-pool MTC model fitting first, followed by three-pool model fitting) using the densely sampled Z-spectra (Fig. 6c) and MRF-SPEM reconstruction using the MRF-SPEM signal profile (Fig. 6d) created by the variable RF saturation are shown in Fig. 6f and g, respectively. The CEST parameter values estimated by MRF-SPEM were in good agreement with values estimated by using the reference measurement in spite of concurrent variation of CEST concentration and pH in each vial (Table 2).

3.3. Human volunteer imaging results

To compare the proposed MRF-SPEM with conventional CEST measurements as a standard for validation of *in-vivo* CEST parameter quantification, Z-spectra were synthesized using estimated parameters from MRF-SPEM and compared with experimentally measured Z-spectra with three different RF saturation powers (1, 1.5, and 2 μT). Fig. 7a shows average ROI-based MRF-SPEM signal evolution profiles (+), and two-pool fitted (solid line), three-pool fitted (dashed line) curves of gray and white matter. The reference signals (solid lines) were calculated by the two-pool MTC model fitting with semisolid MTC data (black crosses

Table 2
Estimated CEST parameters (exchange rates and concentrations) in the presence of MTC (1% agarose) pool from the ammonium chloride phantom study.

		Reference[a]	MRF-SPEM
k_{sw} (Hz): mean ± STD 95% CI	ROI1	2599 ± 51	2592 ± 44
		2585–2613	2586–2598
	ROI2	3876 ± 79	3911 ± 28
		3870–3883	3906–3916
	ROI3	2692 ± 81	2771 ± 37
		2674–2710	2767–2775
M_0^s (mM): mean ± STD 95% CI	ROI1	446 ± 240	460 ± 154
		445–448	451–470
	ROI2	496 ± 74	486 ± 80
		495–496	485–488
	ROI3	1045 ± 197	1075 ± 79
		1043–1046	1072–1079

[a] Reference: a three-pool Bloch equation fitting method using densely sampled Z-spectra with multiple RF saturation powers.

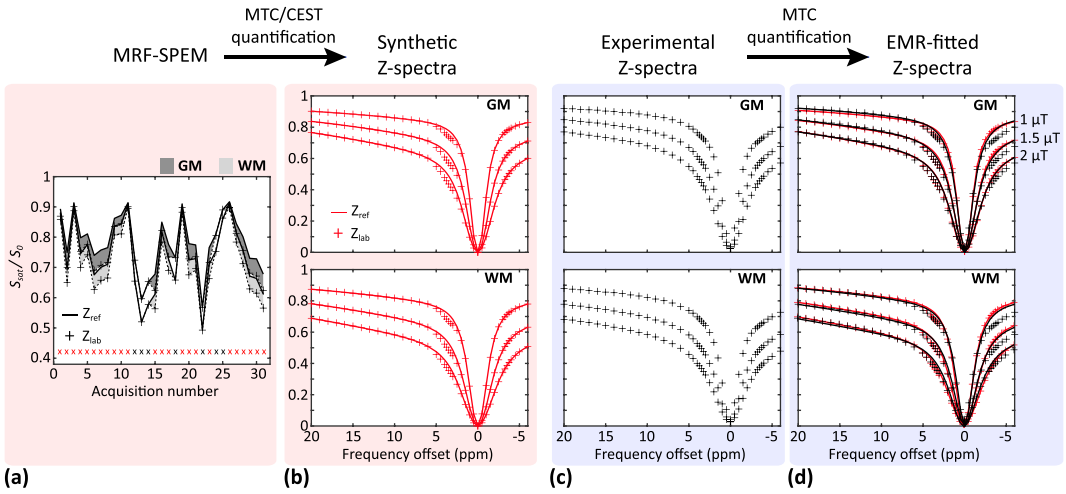

Fig. 7. (a) Average ROI-based MRF-SPEM signal evolution profiles (+), and two-pool fitted (solid lines) and three-pool fitted (dashed lines) curves from white matter and gray matter (n = 5). Note that shaded areas indicate APT effects by subtracting three-pool MRF-SPEM label signals from two-pool MRF-SPEM reference signals. Black and red crosses are two-pool MTC and three-pool APT data acquisitions, respectively. (b) Synthetic two-pool (red solid lines) and three-pool (red +) Z-spectra using quantitative parameters estimated from MRF-SPEM profiles. (c) Experimentally measured conventional Z-spectra with three different RF saturation powers as a standard for validating MRF-SPEM quantification. (d) Experimentally measured conventional Z-spectra (black +) and extrapolated two-pool MTC-fitted curves (Z_{EMR}, black solid lines). Synthetic two-pool (red solid lines) and three-pool (red +) Z-spectra are shown for comparison.

in Fig. 7a). Shaded areas (dark gray and light gray) indicate APT signal effects by subtracting three-pool MRF-SPEM label signals from two-pool MRF-SPEM reference signals. The APT signal intensities were higher in the gray matter than in the white matter. Using CEST parameters estimated from MRF-SPEM, synthetic Z-spectra (Fig. 7b) were reconstructed with saturation/imaging parameters identical to those used in the standard scan (Fig. 7c and d). Synthesized (Fig. 7b) and experimentally measured (Fig. 7c) signals were in excellent agreement at positive frequency offsets (red vs. black solid lines and + signs in Fig. 7d). Note that the synthesized Z_{lab} signals (Fig. 7b) evidently differed from the result of the experimental measurements (Fig. 7c) at negative frequency offsets (upfield from water) because only a three-pool exchange model (free bulk water, semisolid MTC, and downfield amide protons pools) was considered in MRF-SPEM and because the MTC effect was considered symmetric. As shown in Fig. 8a and b, both synthetic Z_{ref} (3.5 ppm) values in gray matter and white matter were in excellent agreement with the EMR results. Interestingly, even though the difference was not statistically significant, the APT$^{\#}$(syn) values seemed slightly higher than the APT$^{\#}$(meas) values, as shown in Fig. 8c, probably because multiple CEST components contaminated the signal at the amide proton frequency (more detail provided in the Discussion section).

Quantitative parameter maps and values of the healthy volunteer brain are shown in Fig. 9 and Table 3. The gray matter and white matter have very different semisolid macromolecular proton and amide proton concentrations and exchange rates. The semisolid macromolecular proton exchange rates for gray and white matter were ~40 Hz (95% confidence interval: 34 Hz–46 Hz) and ~29 Hz (95% confidence interval: 24 Hz–34 Hz), respectively, and the concentrations of ~6 M (95% confidence interval: 5.4 M–7.1 M) and ~11 M (95% confidence interval: 10.3 M–12.1 M), respectively, were in good agreement with previous observations (Mougin et al., 2010; Sled and Pike, 2001; Stanisz et al., 2005). The amide proton concentration in gray matter (266 ± 22 mM; 95% confidence interval: 238 mM–293 mM) was somewhat higher than that of the white matter (212 ± 22 mM; 95% confidence interval: 185 mM–240 mM), which is in line with observed APT effects (shaded areas in Fig. 7a). In addition, the amide proton exchange rate (~365 Hz;

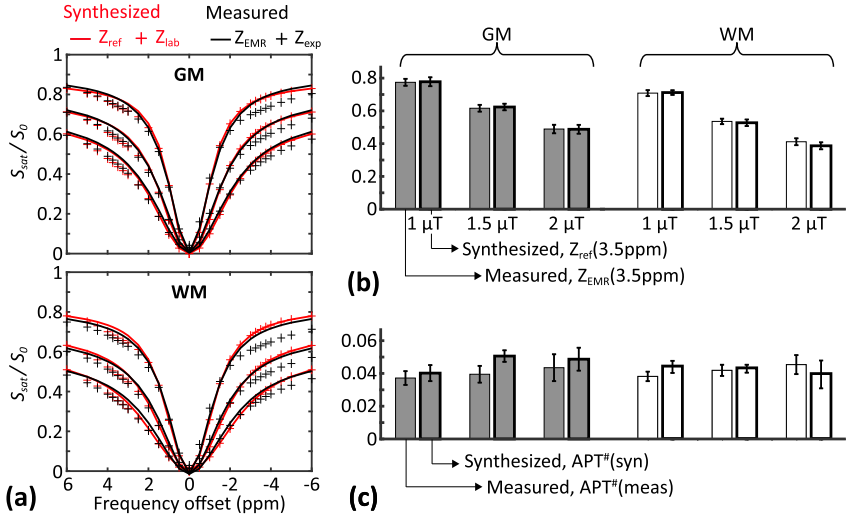

Fig. 8. (a) Average synthesized and experimentally measured Z-spectra from gray matter and white matter. (b) Average experimentally measured Z_{EMR} (3.5 ppm) and synthesized Z_{ref} (3.5 ppm). (c) Experimentally measured APT$^{\#}$(meas) (calculated by Eq. (11)) and synthesized APT$^{\#}$(syn) (calculated by Eq. (10)) image intensities obtained from gray matter and white matter. Error bars depict standard deviations. No values were statistically significant ($p > 0.05$).

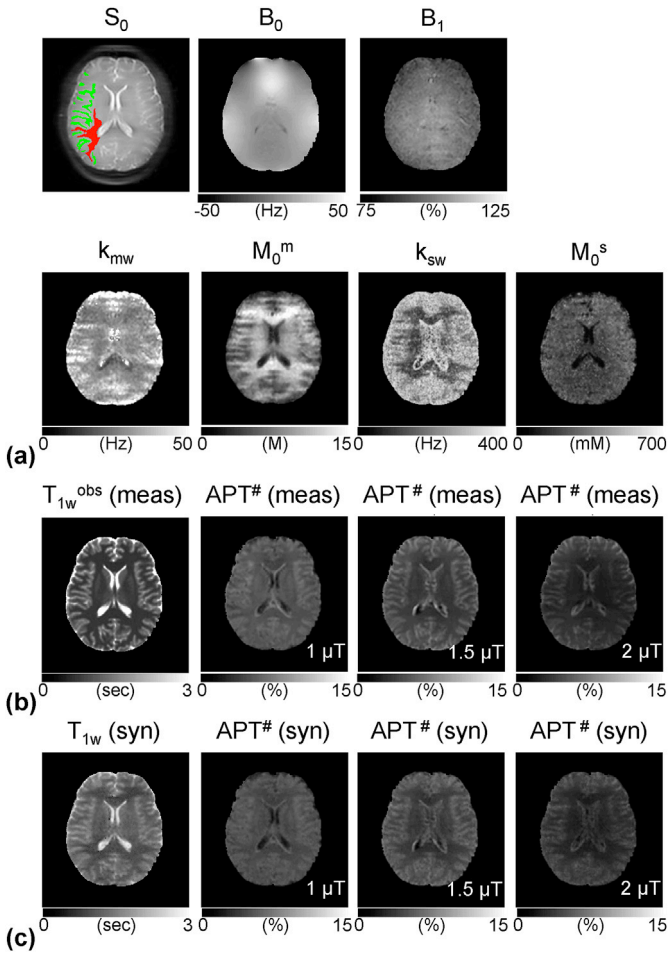

Fig. 9. (a) An unsaturated image with color coded ROIs (green: gray matter, red: white matter) and B_0, B_1, quantitative MTC (k_{mw} and M_0^m), APT (k_{sw} and M_0^s) maps of a representative healthy volunteer human brain. (b) experimentally measured T_1 map (T_{1w}^{obs}) from a modified look-locker inversion recovery and APT$^{\#}$(meas) images with RF saturation powers of 1, 1.5, and 2 μT. (c) Synthetic T_1 map (T_{1w} (syn)) and APT$^{\#}$(syn) images with RF saturation powers of 1, 1.5, and 2 μT.

95% confidence interval: 342 Hz–389 Hz) of gray matter was significantly faster than that of white matter (~162 Hz; 95% confidence interval: 142 Hz–182 Hz). All differences in the amide proton exchange rates and concentrations between the gray matter and white matter were significant ($p < 0.05$, see Table 3). Synthesized APT$^{\#}$ images were in good agreement with the experimentally measured APT$^{\#}$ images as shown in Fig. 9b and c. However, the intrinsic water T_1 relaxation time of the white matter calculated from MRF-SPEM reconstruction was longer than the observed water T_1 relaxation time of the white matter obtained from a modified look-locker inversion recovery experiment due to the effect of coupling to a semisolid macromolecular proton pool (Henkelman et al., 1993).

4. Discussion

We developed a novel MRF concept to allow CEST quantification by SPEM. Numerical phantom studies demonstrated that MRF-SPEM can enable a high degree of accuracy and precision in absolute CEST quantification at 3T magnetic field strength. The same model used *in-vivo* allowed fast quantification of apparent exchange rates and concentrations at the amide proton frequency. The present MRF-SPEM imaging scan took just 2 min 50 s (including B_0 and B_1 mapping) for quantitative APT mapping (as compared to 11 min 12 s for EMR image acquisition

Table 3
Estimated free bulk water, semisolid MTC, and APT parameters for white matter and gray matter of the healthy volunteer human brain.

No.	T_{1w} (sec)		T_{2w} (msec)		T_{2m} (μsec)		k_{mw} (Hz)		M_0^m (M)		T_{2s} (msec)		k_{sw} (Hz)		M_0^s (mM)	
	WM	GM	WM	GM	WM	GM	WM	GM	WM	GM	WM	GM	WM	GM	WM	GM
1	0.99	1.10	35.0	70.5	58	61	23	33	11.9	7.0	2.5	0.9	151	353	198	299
2	1.05	1.29	39.4	67.0	62	64	26	36	10.8	6.8	2.2	1.3	141	380	235	241
3	1.07	1.34	42.0	77.0	61	67	31	44	11.9	5.4	1.8	0.8	181	390	234	256
4	1.06	1.05	44.8	77.0	68	71	31	42	10.3	5.7	2.0	0.9	168	346	185	276
5	1.05	1.30	37.8	65.1	67	72	33	44	11.0	6.5	1.9	1.7	171	357	209	256
mean ± STD	1.05 ± 0.03	1.21 ± 0.13	39.8 ± 3.8	71.3 ± 5.6	63 ± 4	67 ± 5	29 ± 4	40 ± 5	11.2 ± 0.7	6.3 ± 0.7	2.1 ± 0.3	1.1 ± 0.4	162 ± 16	365 ± 19	212 ± 22	266 ± 22
95% CI	1.01–1.08	1.05–1.38	35.1–44.5	64.4–78.3	58–68	61–73	24–34	34–46	10.3–12.1	5.4–7.1	1.7–2.4	0.7–1.6	142–182	342–389	185–240	238–293
p-value	0.0330		<0.001		0.0097		<0.001		<0.001		0.0112		<0.001		0.0458	

with three RF saturation powers).

Our proposed method cannot be systematically assessed in-vitro and in-vivo due to the lack of an objective ground-truth. To enable effective validation, in lieu of ground-truth, we compared MRF-SPEM with a conventional Bloch equation fitting method with high-resolution Z-spectra using ammonium chloride-agarose phantoms and observed great agreement between the two measurements for the proton quantification. However, the estimated proton exchange rates were higher than the value reported in a previous ammonium chloride phantom study with similar pH ranges (Desmond and Stanisz, 2012). We observed broadened CEST peaks with significant asymmetry in the Z-spectra due to coalescence of the fast exchanging proton peaks with the bulk water peak. Presumably, a change in pH during the phantom preparation (e.g., boiling for the agarose) may lead to a change in the lineshape of Z-spectra. In the human study, synthesized Z-spectra and $APT^{\#}$ images generated with CEST parameters estimated from MRF-SPEM were in good agreement with the experimental measurements in white matter and gray matter regions of the healthy volunteer brain at 3 T. A fast exchange rate of semisolid macromolecular and amide protons was observed in voxels located partly in the cerebral ventricles (cerebrospinal fluid) with long T_1 relaxation times. However, previous studies showed that APT signal of the CSF is almost zero and independent of RF saturation power, thus the APT effect can be assumed to be negligible in the ventricles (Paech et al., 2014; Zhao et al., 2011; also see simulation results in Supporting Fig. S1). In addition, there should be no MTC in the ventricles and these APT and MTC effects are only apparent and due to partial volume effects with tissue and perhaps CSF flow-related effects.

We investigated the spatial distribution of the magnitude of MTC and APT effects in the human brain. While the estimated semisolid macromolecular proton concentration was significantly larger in white matter than in gray matter, the exchange rate was significantly faster in gray matter than in white matter. The estimated semisolid macromolecular proton parameters by MRF-SPEM were consistent with previous quantitative MT studies (Mougin et al., 2010; Sled and Pike, 2001; Stanisz et al., 2005). The APT signals were found to be slightly higher in gray matter than in white matter, in line with previous experiments (Jin et al., 2013; Xu et al., 2016), presumably as a result of the higher content of mobile proteins and peptides, or the greater magnetization exchange between protons in the water and macromolecular pools in white matter, leaving fewer water protons for exchange with mobile proteins and peptides. The apparent amide proton exchange rates of the gray matter and white matter estimated from MRF-SPEM were around 162 Hz and 365 Hz, respectively. Our APT quantification values were high compared to the values of the exchange rates and concentration (~28 Hz and 72 mM) reported in previous rat animal studies at 4.7 T using a water-exchange spectroscopy (WEX) approach (Mori et al., 1997; Zhou et al., 2003b, 2004). One possible reason for this lack of consensus is that the amide protons have a wide range of exchange rates, while the model used here assumed that the amide protons had a single exchange rate. Amide protons in proteins and peptides are known to exhibit a large range of exchange rates at a physiologically relevant pH range (Wuthrich, 1986). The WEX approach may be less suitable for measuring very fast exchange rates due to the finite duration (several ms) of the water labeling preparation period. In the previous study, furthermore, the amide proton concentration (72 mM) was retrospectively calculated from a simplified two-pool exchange model-based APT ratio equation with the exchange rate of 28 Hz measured from WEX experiment. Another less likely possibility is that multiple CEST components can influence the signal at the amide proton frequency offset. At 3T, even with the low RF saturation power pulse, there may still be some contamination from broad coalesced signals of amine protons from glutamate (Cai et al., 2012; Zhang et al., 2018), guanidinium protons from creatine and mobile protein/peptide (Haris et al., 2012; Zhang et al., 2017c), and hydroxyl protons from myo-inositol (Haris et al., 2011), glycogen (van Zijl et al., 2007), and glycosaminoglycans (Ling et al., 2008) over the amide proton frequency. Note that a previous human study at 7T (Liu et al., 2013) measured the amide proton exchange rate of ~280 Hz, which is comparable to that measured here, while the concentration was somewhat lower than our estimation. A human study using the frequency labeled exchange approach measured a rate on the order of 350–400 Hz (Yadav et al., 2013). Another human study (Geades et al., 2017) measured the amide proton concentration of 220 mM (0.2% relative to water, 110M), which is consistent with that measured in this work.

Finding a unique (or sparse) solution in an ill-posed inverse problem is always challenging, particularly when multiple components for CEST MRI are considered. To overcome this issue, we shrank the exchange model and reduced fitting parameters by subgrouping proton exchange models. Additional information/constraints, such as different RF saturation powers, saturation times, and frequency offsets were added to find a unique solution (CEST parameters). Nevertheless, the coupled effect from the exchange rate and concentration was often observed, particularly as shown in k_{mw} and M_0^m maps (Fig. 9a). The high k_{mw} (bright) and low M_0^m (dark) values were shown in the anterior and posterior edges whereas the T_{1w}^{obs}, $APT^{\#}$ (Fig. 9b) and $k_{mw}.M_0^m$ images (see Supporting Fig. S2) showed structures. These CEST-related parameters appear multiplied together in the Bloch equations and thus, it may be difficult to completely disentangle the coupled parameters. In future work, more MTC image acquisitions with varied RF saturation parameters may be required. In addition, the application of a varied inter-pulse delay time (Xu et al., 2014a) may be added to limit CEST signals only to those from biomolecules with a specific range of proton exchange rate to MRF-SPEM. This may yield more reliable CEST parameter mapping, especially when incorporating fast exchangeable amine and guanidinium proton pools in the analysis. Upfield NOE-related proton pools can be easily incorporated into MRF-SPEM because NOE signals are easily discriminated from downfield CEST signals due to the difference in saturation frequency offsets. Nevertheless, including additional proton pools in the model inevitably results in increasing acquisition images and scan time. Currently, an acquisition schedule with 32 image acquisitions was chosen, which is the similar acquisition number used in previous works (Cohen et al., 2018; Zhou et al., 2018). However, future studies are needed to optimize acquisition schedules for reducing acquisition times and maximizing specificity of CEST components.

In the present study, MRF-SPEM data were reconstructed by solving a nonlinear least squares problem, rather than a dictionary-match approach used in the original MRF approach. The advantage of this approach is that an exhaustive brute-force dictionary generation for high precision and search can be avoided, enabling straightforward extensions of the proton exchange model to incorporate multiple CEST parameters without a new dictionary construction. In addition, the use of highly undersampled k-space and short TRs for transient-state signal acquisition, as used in the original MRF may be limited in CEST MRI due to inherently low SNR. Currently, dictionary-free or undersampled/fully sampled Cartesian MRF methods are being explored (Anderson et al., 2018; Buonincontri and Sawiak, 2016; Cohen et al., 2018; Sbrizzi et al., 2017; Zhang et al., 2017b; Zhou et al., 2018). In MRF-SPEM reconstruction, CEST parameter mapping with two-dimensional data (256^2) took about 6 h. Furthermore, the three-pool model might not be enough for in-vivo. Additional CEST pools could be incorporated in MRF-SPEM reconstruction, but it inevitably leads to longer reconstruction times. Recently, much effort has been focused on the compression of the dictionary computation and acceleration of the dictionary matching (Asslander et al., 2018; Cao et al., 2017; Cauley et al., 2015; Cline et al., 2017; McGivney et al., 2014). Such an accelerated dictionary-based, pattern--matching approach could benefit fast three-dimensional MRF-SPEM reconstruction due to the inherent robustness of the dictionary matching to aliasing artifacts.

5. Conclusion

A fast quantitative CEST imaging technique based on MRF-SPEM was developed, validated in numerical phantoms, and demonstrated *in-vivo*

using a synthetic CEST analysis. This quantitative approach could provide significant insights into the origin of the conventional CEST-weighted image contrast in normal human brains and in many pathologies, such as cancer, stroke, and various psychiatric and neurodegenerative diseases.

Acknowledgment

The authors thank Drs. Nirbhay Yadav and Yi Zhang for helpful discussions and Dr. Guanshu Liu for the support in the construction of the phantom. This work was supported in part by grants from the National Institutes of Health (R01EB009731, R01CA166171, R01CA228188, R01EB015032, R21CA227783, UG3NS106931, and P41EB015909).

Appendix A. Supplementary data

Supplementary data to this article can be found online at https://doi.org/10.1016/j.neuroimage.2019.01.034.

References

Aime, S., Calabi, L., Biondi, L., De Miranda, M., Ghelli, S., Paleari, L., Rebaudengo, C., Terreno, E., 2005. Iopamidol: exploring the potential use of a well-established x-ray contrast agent for MRI. Magn. Reson. Med. 53, 830–834.

Anderson, C.E., Wang, C.Y., Gu, Y., Darrah, R., Griswold, M.A., Yu, X., Flask, C.A., 2018. Regularly incremented phase encoding - MR fingerprinting (RIPE-MRF) for enhanced motion artifact suppression in preclinical cartesian MR fingerprinting. Magn. Reson. Med. 79, 2176–2182.

Asslander, J., Cloos, M.A., Knoll, F., Sodickson, D.K., Hennig, J., Lattanzi, R., 2018. Low rank alternating direction method of multipliers reconstruction for MR fingerprinting. Magn. Reson. Med. 79, 83–96.

Buonincontri, G., Sawiak, S.J., 2016. MR fingerprinting with simultaneous B1 estimation. Magn. Reson. Med. 76, 1127–1135.

Cai, K., Singh, A., Poptani, H., Li, W., Yang, S., Lu, Y., Hariharan, H., Zhou, X.J., Reddy, R., 2015. CEST signal at 2ppm (CEST@2ppm) from Z-spectral fitting correlates with creatine distribution in brain tumor. NMR Biomed. 28, 1–8.

Cai, K.J., Haris, M., Singh, A., Kogan, F., Greenberg, J.H., Hariharan, H., Detre, J.A., Reddy, R., 2012. Magnetic resonance imaging of glutamate. Nat. Med. 18, 302–306.

Cao, X., Liao, C., Wang, Z., Chen, Y., Ye, H., He, H., Zhong, J., 2017. Robust sliding-window reconstruction for Accelerating the acquisition of MR fingerprinting. Magn. Reson. Med. 78, 1579–1588.

Cauley, S.F., Setsompop, K., Ma, D., Jiang, Y., Ye, H., Adalsteinsson, E., Griswold, M.A., Wald, L.L., 2015. Fast group matching for MR fingerprinting reconstruction. Magn. Reson. Med. 74, 523–528.

Cline, C.C., Chen, X., Mailhe, B., Wang, Q., Pfeuffer, J., Nittka, M., Griswold, M.A., Speier, P., Nadar, M.S., 2017. AIR-MRF: accelerated iterative reconstruction for magnetic resonance fingerprinting. Magn. Reson. Imaging 41, 29–40.

Cohen, O., Huang, S., McMahon, M.T., Rosen, M.S., Farrar, C.T., 2018. Rapid and quantitative chemical exchange saturation transfer (CEST) imaging with magnetic resonance fingerprinting (MRF). Magn. Reson. Med. https://doi.org/10.1002/mrm.27221.

Desmond, K.L., Stanisz, G.J., 2012. Understanding quantitative pulsed CEST in the presence of MT. Magn. Reson. Med. 67, 979–990.

Geades, N., Hunt, B.A.E., Shah, S.M., Peters, A., Mougin, O.E., Gowland, P.A., 2017. Quantitative analysis of the z-spectrum using a numerically simulated look-up table: application to the healthy human brain at 7T. Magn. Reson. Med. 78, 645–655.

Goffeney, N., Bulte, J.W.M., Duyn, J., Bryant, L.H., van Zijl, P.C.M., 2001. Sensitive NMR detection of cationic-polymer-based gene delivery systems using saturation transfer via proton exchange. J. Am. Chem. Soc. 123, 8628–8629.

Haris, M., Cai, K., Singh, A., Hariharan, H., Reddy, R., 2011. In vivo mapping of brain myo-inositol. Neuroimage 54, 2079–2085.

Haris, M., Nanga, R.P., Singh, A., Cai, K., Kogan, F., Hariharan, H., Reddy, R., 2012. Exchange rates of creatine kinase metabolites: feasibility of imaging creatine by chemical exchange saturation transfer MRI. NMR Biomed. 25, 1305–1309.

Haris, M., Singh, A., Cai, K., Kogan, F., McGarvey, J., Debrosse, C., Zsido, G.A., Witschey, W.R., Koomalsingh, K., Pilla, J.J., Chirinos, J.A., Ferrari, V.A., Gorman, J.H., Hariharan, H., Gorman, R.C., Reddy, R., 2014. A technique for in vivo mapping of myocardial creatine kinase metabolism. Nat. Med. 20, 209–214.

Henkelman, R.M., Huang, X., Xiang, Q.S., Stanisz, G.J., Swanson, S.D., Bronskill, M.J., 1993. Quantitative interpretation of magnetization transfer. Magn. Reson. Med. 29, 759–766.

Heo, H.Y., Jones, C.K., Hua, J., Yadav, N., Agarwal, S., Zhou, J., van Zijl, P.C., Pillai, J.J., 2016a. Whole-brain amide proton transfer (APT) and nuclear overhauser enhancement (NOE) imaging in glioma patients using low-power steady-state pulsed chemical exchange saturation transfer (CEST) imaging at 7T. J. Magn. Reson. Imag. 44, 41–50.

Heo, H.Y., Lee, D.H., Zhang, Y., Zhao, X., Jiang, S., Chen, M., Zhou, J., 2017a. Insight into the quantitative metrics of chemical exchange saturation transfer (CEST) imaging. Magn. Reson. Med. 77, 1853–1865.

Heo, H.Y., Zhang, Y., Burton, T.M., Jiang, S., Zhao, Y., van Zijl, P.C.M., Leigh, R., Zhou, J., 2017b. Improving the detection sensitivity of pH-weighted amide proton transfer MRI in acute stroke patients using extrapolated semisolid magnetization transfer reference signals. Magn. Reson. Med. 78, 871–880.

Heo, H.Y., Zhang, Y., Jiang, S., Lee, D.H., Zhou, J., 2016b. Quantitative assessment of amide proton transfer (APT) and nuclear overhauser enhancement (NOE) imaging with extrapolated semisolid magnetization transfer reference (EMR) signals: II. Comparison of three EMR models and application to human brain glioma at 3 Tesla. Magn. Reson. Med. 75, 1630–1639.

Heo, H.Y., Zhang, Y., Jiang, S., Zhou, J., 2018. Influences of experimental parameters on chemical exchange saturation transfer (CEST) metrics of brain tumors using animal models at 4.7T. Magn. Reson. Med. https://doi.org/10.1002/mrm.27389.

Heo, H.Y., Zhang, Y., Lee, D.H., Hong, X., Zhou, J., 2016c. Quantitative assessment of amide proton transfer (APT) and nuclear overhauser enhancement (NOE) imaging with extrapolated semi-solid magnetization transfer reference (EMR) signals: application to a rat glioma model at 4.7 tesla. Magn. Reson. Med. 75, 137–149.

Heo, H.Y., Zhang, Y., Lee, D.H., Jiang, S., Zhao, X., Zhou, J., 2017c. Accelerating chemical exchange saturation transfer (CEST) MRI by combining compressed sensing and sensitivity encoding techniques. Magn. Reson. Med. 77, 779–786.

Hua, J., Jones, C.K., Blakeley, J., Smith, S.A., van Zijl, P.C., Zhou, J., 2007. Quantitative description of the asymmetry in magnetization transfer effects around the water resonance in the human brain. Magn. Reson. Med. 58, 786–793.

Jiang, S., Eberhart, C.G., Zhang, Y., Heo, H.-Y., Wen, Z., Blair, L., Qin, H., Lim, M., Quinones-Hinojosa, A., Weingart, J.D., Barker, P.B., Pomper, M.G., Laterra, J., van Zijl, P.C.M., Blakeley, J.O., Zhou, J., 2017. Amide proton transfer-weighted MR image-guided stereotactic biopsy in patients with newly diagnosed gliomas. Eur. J. Cancer 83, 9–18.

Jin, T., Wang, P., Zong, X., Kim, S.G., 2013. MR imaging of the amide-proton transfer effect and the pH-insensitive nuclear overhauser effect at 9.4 T. Magn. Reson. Med. 69, 760–770.

Jin, T., Wang, P., Zong, X.P., Kim, S.G., 2012. Magnetic resonance imaging of the Amine-Proton EXchange (APEX) dependent contrast. Neuroimage 59, 1218–1227.

Jones, C.K., Huang, A., Xu, J., Edden, R.A., Schar, M., Hua, J., Oskolkov, N., Zaca, D., Zhou, J., McMahon, M.T., Pillai, J.J., van Zijl, P.C., 2013. Nuclear Overhauser enhancement (NOE) imaging in the human brain at 7T. Neuroimage 77, 114–124.

Jones, K.M., Randtke, E.A., Yoshimaru, E.S., Howison, C.M., Chalasani, P., Klein, R.R., Chambers, S.K., Kuo, P.H., Pagel, M.D., 2017. Clinical translation of tumor acidosis measurements with AcidoCEST MRI. Mol. Imag. Biol. 19, 617–625.

Kim, M., Gillen, J., Landman, B.A., Zhou, J., van Zijl, P.C., 2009. Water saturation shift referencing (WASSR) for chemical exchange saturation transfer (CEST) experiments. Magn. Reson. Med. 61, 1441–1450.

Lee, D.H., Heo, H.Y., Zhang, K., Zhang, Y., Jiang, S., Zhao, X., Zhou, J., 2017. Quantitative assessment of the effects of water proton concentration and water T1 changes on amide proton transfer (APT) and nuclear overhauser enhancement (NOE) MRI: the origin of the APT imaging signal in brain tumor. Magn. Reson. Med. 77, 855–863.

Li, C., Peng, S., Wang, R., Chen, H., Su, W., Zhao, X., Zhou, J., Chen, M., 2014. Chemical exchange saturation transfer MR imaging of Parkinson's disease at 3 Tesla. Eur. Radiol. 24, 2631–2639.

Liao, C., Bilgic, B., Manhard, M.K., Zhao, B., Cao, X., Zhong, J., Wald, L.L., Setsompop, K., 2017. 3D MR fingerprinting with accelerated stack-of-spirals and hybrid sliding-window and GRAPPA reconstruction. Neuroimage 162, 13–22.

Ling, W., Regatte, R.R., Navon, G., Jerschow, A., 2008. Assessment of glycosaminoglycan concentration in vivo by chemical exchange-dependent saturation transfer (gagCEST). Proc. Natl. Acad. Sci. Unit. States Am. 105, 2266–2270.

Liu, D., Zhou, J., Xue, R., Zuo, Z., An, J., Wang, D.J.J., 2013. Quantitative characterization of nuclear Overhauser enhancement and amide proton transfer effects in the human brain at 7 Tesla. Magn. Reson. Med. 70, 1070–1081.

Ma, D., Gulani, V., Seiberlich, N., Liu, K., Sunshine, J.L., Duerk, J.L., Griswold, M.A., 2013. Magnetic resonance fingerprinting. Nature 495, 187–192.

Ma, D., Jiang, Y., Chen, Y., McGivney, D., Mehta, B., Gulani, V., Griswold, M., 2017. Fast 3D magnetic resonance fingerprinting for a whole-brain coverage. Magn. Reson. Med. https://doi.org/10.1002/mrm.26886.

McGivney, D.F., Pierre, E., Ma, D., Jiang, Y., Saybasili, H., Gulani, V., Griswold, M.A., 2014. SVD compression for magnetic resonance fingerprinting in the time domain. IEEE Trans. Med. Imag. 33, 2311–2322.

McMahon, M.T., Gilad, A.A., Zhou, J., Sun, P.Z., Bulte, J.W.M., van Zijl, P.C.M., 2006. Quantifying exchange rates in chemical exchange saturation transfer agents using the saturation time and saturation power dependencies of the magnetization transfer effect on the magnetic resonance imaging signal (QUEST and QUESP): pH calibration for poly-L-lysine and a starburst dendrimer. Magn. Reson. Med. 55, 836–847.

Mori, S., Abeygunawardana, C., Berg, J.M., van Zijl, P.C.M., 1997. NMR study of rapidly exchanging backbone amide protons in staphylococcal nuclease and the correlation with structural and dynamic properties. J. Am. Chem. Soc. 119, 6844–6852.

Mougin, O.E., Coxon, R.C., Pitiot, A., Gowland, P.A., 2010. Magnetization transfer phenomenon in the human brain at 7T. Neuroimage 49, 272–281.

Paech, D., Zaiss, M., Meissner, J.E., Windschuh, J., Wiestler, B., Bachert, P., Neumann, J.O., Kickingereder, P., Schlemmer, H.P., Wick, W., Nagel, A.M., Heiland, S., Ladd, M.E., Bendszus, M., Radbruch, A., 2014. Nuclear overhauser enhancement mediated chemical exchange saturation transfer imaging at 7 Tesla in glioblastoma patients. PLoS One 9, e104181.

Sbrizzi, A., Bruijn, T., van der Heide, O., Luijten, P., van den Berg, C.A.T., 2017. Dictionary-free MR Fingerprinting Reconstruction of Balanced-GRE Sequences. 1711.08905.

Sled, J.G., Pike, G.B., 2001. Quantitative imaging of magnetization transfer exchange and relaxation properties in vivo using MRI. Magn. Reson. Med. 46, 923–931.

Stanisz, G.J., Odrobina, E.E., Pun, J., Escaravage, M., Graham, S.J., Bronskill, M.J., Henkelman, R.M., 2005. T-1, T-2 relaxation and magnetization transfer in tissue at 3T. Magn. Reson. Med. 54, 507–512.

Su, P., Mao, D., Liu, P., Li, Y., Pinho, M.C., Welch, B.G., Lu, H., 2017. Multiparametric estimation of brain hemodynamics with MR fingerprinting ASL. Magn. Reson. Med. 78, 1812–1823.
Sun, P.Z., Lu, J., Wu, Y., Xiao, G., Wu, R., 2013. Evaluation of the dependence of CEST-EPI measurement on repetition time, RF irradiation duty cycle and imaging flip angle for enhanced pH sensitivity. Phys. Med. Biol. 58, N229–N240.
Sun, P.Z., Zhou, J., Sun, W., Huang, J., van Zijl, P.C.M., 2007. Detection of the ischemic penumbra using pH-weighted MRI. J. Cerebr. Blood Flow Metabol. 27, 1129–1136.
van Zijl, P.C.M., Jones, C.K., Ren, J., Malloy, C.R., Sherry, A.D., 2007. MRI detection of glycogen in vivo by using chemical exchange saturation transfer imaging (glycoCEST). Proc. Natl. Acad. Sci. Unit. States Am. 104, 4359–4364.
van Zijl, P.C.M., Lam, W.W., Xu, J., Knutsson, L., Stanisz, G.J., 2018. Magnetization transfer contrast and chemical exchange saturation transfer MRI. Features and analysis of the field-dependent saturation spectrum. Neuroimage 168, 222–241.
van Zijl, P.C.M., Yadav, N.N., 2011. Chemical exchange saturation transfer (CEST): what is in a name and what isn't? Magn. Reson. Med. 65, 927–948.
van Zijl, P.C.M., Zhou, J., Mori, N., Payen, J.F., Wilson, D., Mori, S., 2003. Mechanism of magnetization transfer during on-resonance water saturation. A new approach to detect mobile proteins, peptides, and lipids. Magn. Reson. Med. 49, 440–449.
Walker-Samuel, S., Ramasawmy, R., Torrealdea, F., Rega, M., Rajkumar, V., Johnson, S.P., Richardson, S., Goncalves, M., Parkes, H.G., Arstad, E., Thomas, D.L., Pedley, R.B., Lythgoe, M.F., Golay, X., 2013. In vivo imaging of glucose uptake and metabolism in tumors. Nat. Med. 19, 1067–1072.
Wang, C.Y., Liu, Y., Huang, S., Griswold, M.A., Seiberlich, N., Yu, X., 2017. (31) P magnetic resonance fingerprinting for rapid quantification of creatine kinase reaction rate in vivo. NMR Biomed. 30, e3786.
Ward, K.M., Aletras, A.H., Balaban, R.S., 2000. A new class of contrast agents for MRI based on proton chemical exchange dependent saturation transfer (CEST). J. Magn. Reson. 143, 79–87.
Woessner, D.E., Zhang, S., Merritt, M.E., Sherry, A.D., 2005. Numerical solution of the Bloch equations provides insights into the optimum design of PARACEST agents for MRI. Magn. Reson. Med. 53, 790–799.
Wuthrich, K., 1986. NMR of Proteins and Nucleic Acids, 2 ed. John Wiley & Sons, New York.
Xu, J., Yadav, N.N., Bar-Shir, A., Jones, C.K., Chan, K.W., Zhang, J., Walczak, P., McMahon, M.T., van Zijl, P.C.M., 2014a. Variable delay multi-pulse train for fast chemical exchange saturation transfer and relayed-nuclear overhauser enhancement MRI. Magn. Reson. Med. 71, 1798–1812.
Xu, J., Zaiss, M., Zu, Z., Li, H., Xie, J., Gochberg, D.F., Bachert, P., Gore, J.C., 2014b. On the origins of chemical exchange saturation transfer (CEST) contrast in tumors at 9.4 T. NMR Biomed. 27, 406–416.
Xu, X., Yadav, N.N., Zeng, H., Jones, C.K., Zhou, J., van Zijl, P.C.M., Xu, J., 2016. Magnetization transfer contrast-suppressed imaging of amide proton transfer and relayed nuclear overhauser enhancement chemical exchange saturation transfer effects in the human brain at 7T. Magn. Reson. Med. 75, 88–96.
Yadav, N.N., Jones, C.K., Hua, J., Xu, J., van Zijl, P.C.M., 2013. Imaging of endogenous exchangeable proton signals in the human brain using frequency labeled exchange transfer imaging. Magn. Reson. Med. 69, 966–973.
Zaiss, M., Schmitt, B., Bachert, P., 2011. Quantitative separation of CEST effect from magnetization transfer and spillover effects by Lorentzian-line-fit analysis of z-spectra. J. Magn. Reson. 211, 149–155.
Zhang, H., Kang, H., Zhao, X., Jiang, S., Zhang, Y., Zhou, J., Peng, Y., 2016a. Amide proton transfer (APT) MR imaging and magnetization transfer (MT) MR imaging of pediatric brain development. Eur. Radiol. 26, 3368–3376.
Zhang, H., Wang, W., Jiang, S., Zhang, Y., Heo, H.Y., Wang, X., Peng, Y., Wang, J., Zhou, J., 2017a. Amide proton transfer-weighted MRI detection of traumatic brain injury in rats. J. Cerebr. Blood Flow Metabol. 37, 3422–3432.
Zhang, S., Winter, P., Wu, K., Sherry, A.D., 2001. A novel europium(III)-based MRI contrast agent. J. Am. Chem. Soc. 123, 1517–1578.
Zhang, S.R., Malloy, C.R., Sherry, A.D., 2005. MRI thermometry based on PARACEST agents. J. Am. Chem. Soc. 127, 17572–17573.
Zhang, X., Zhou, Z., Chen, S., Li, R., Hu, X., 2017b. MR fingerprinting reconstruction with Kalman filter. Magn. Reson. Imaging 41, 53–62.
Zhang, X.Y., Wang, F., Li, H., Xu, J., Gochberg, D.F., Gore, J.C., Zu, Z., 2017c. Accuracy in the quantification of chemical exchange saturation transfer (CEST) and relayed nuclear Overhauser enhancement (rNOE) saturation transfer effects. NMR Biomed. 30, e3716.
Zhang, X.Y., Wang, F., Xu, J., Gochberg, D.F., Gore, J.C., Zu, Z., 2018. Increased CEST specificity for amide and fast-exchanging amine protons using exchange-dependent relaxation rate. NMR Biomed. 31, e3863.
Zhang, X.Y., Xie, J., Wang, F., Lin, E.C., Xu, J., Gochberg, D.F., Gore, J.C., Zu, Z., 2017d. Assignment of the molecular origins of CEST signals at 2 ppm in rat brain. Magn. Reson. Med. 78, 881–887.
Zhang, Y., Heo, H.Y., Lee, D.H., Zhao, X., Jiang, S., Zhang, K., Li, H., Zhou, J., 2016b. Selecting the reference image for registration of CEST series. J. Magn. Reson. Imag. 43, 756–761.
Zhao, X., Wen, Z., Huang, F., Lu, S., Wang, X., Hu, S., Zu, D., Zhou, J., 2011. Saturation power dependence of amide proton transfer image contrasts in human brain tumors and strokes at 3 T. Magn. Reson. Med. 66, 1033–1041.
Zhou, J., Blakeley, J.O., Hua, J., Kim, M., Laterra, J., Pomper, M.G., van Zijl, P.C.M., 2008. Practical data acquisition method for human brain tumor amide proton transfer (APT) imaging. Magn. Reson. Med. 60, 842–849.
Zhou, J., Hong, X., Zhao, X., Gao, J.H., Yuan, J., 2013a. APT-weighted and NOE-weighted image contrasts in glioma with different RF saturation powers based on magnetization transfer ratio asymmetry analyses. Magn. Reson. Med. 70, 320–327.
Zhou, J., Lal, B., Wilson, D.A., Laterra, J., van Zijl, P.C.M., 2003a. Amide proton transfer (APT) contrast for imaging of brain tumors. Magn. Reson. Med. 50, 1120–1126.
Zhou, J., Payen, J., Wilson, D.A., Traystman, R.J., van Zijl, P.C.M., 2003b. Using the amide proton signals of intracellular proteins and peptides to detect pH effects in MRI. Nat. Med. 9, 1085–1090.
Zhou, J., van Zijl, P.C.M., 2006. Chemical exchange saturation transfer imaging and spectroscopy. Progr. NMR Spectr. 48, 109–136.
Zhou, J., Wilson, D.A., Sun, P.Z., Klaus, J.A., Van Zijl, P.C.M., 2004. Quantitative description of proton exchange processes between water and endogenous and exogenous agents for WEX, CEST, and APT experiments. Magn. Reson. Med. 51, 945–952.
Zhou, J., Zhu, H., Lim, M., Blair, L., Quinones-Hinojosa, A., Messina, A.A., Eberhart, C.G., Pomper, M.G., Laterra, J., Barker, P.B., van Zijl, P.C.M., Blakeley, J.O., 2013b. Three-dimensional amide proton transfer MR imaging of gliomas: initial experience and comparison with gadolinium enhancement. J. Magn. Reson. Imag. 38, 1119–1128.
Zhou, Z., Han, P., Zhou, B., Christodoulou, A.G., Shaw, J.L., Deng, Z., Li, D., 2018. Chemical exchange saturation transfer fingerprinting for exchange rate quantification. Magn. Reson. Med. 80, 1352–1363.